

Dual semi-Dirac cones in three-dimensional photonic crystals

Mingyan Li,^{1,5} Ran Mei,^{1,5} Dongyang Yan,^{1,5} Zhikai Ma,³ Fang Cao,⁴ Yadong Xu,^{1,5}
Changqing Xu^{⊗,2,*} and Jie Luo^{⊗,1,5,†}

¹*Institute of Theoretical and Applied Physics, School of Physical Science and Technology, Soochow University, Suzhou 215006, China*

²*School of Physics and Technology, Nanjing Normal University, Nanjing 210023, China*

³*State Key Laboratory for Mesoscopic Physics and Frontiers Science Center for Nano-optoelectronics, School of Physics, Peking University, Beijing 100871, China*

⁴*Laboratory Development and Management Centre & School of Optical and Electronic Information, Suzhou City University, Suzhou 215104, China*

⁵*Provincial Key Lab of Thin Films, Soochow University, Suzhou 215006, China*



(Received 11 January 2024; revised 5 March 2024; accepted 12 March 2024; published 27 March 2024)

Semi-Dirac cones, characterized by linear-parabolic dispersions, endow photonic crystals with many fascinating properties, such as topological transitions and anisotropic electromagnetic responses. While most preceding investigations concentrated on two-dimensional systems, our exploration of three-dimensional photonic crystals comprising a cubic lattice of core-shell spheroids unveils unusual dispersions in three-dimensional systems—dual semi-Dirac cones. The dual semi-Dirac cones arising from a pair of coexisting triply degenerate modes can be analyzed by effective-Hamiltonian and effective-medium theory, accompanied by topological transitions in equal-frequency surfaces and significant changes in electromagnetic responses. We find that the photonic crystal exhibits highly anisotropic wave transport properties, i.e., drastically different transport properties for waves of different wave-vector directions, within the frequency region between the two semi-Dirac frequencies. However, at the frequencies of semi-Dirac points, the photonic crystal behaves as an effective double-zero medium for two propagation directions, but as a single-zero medium for the remaining direction, specifically for orthogonal polarizations. Our findings contribute valuable insights into three-dimensional artificial materials, presenting features absent in two-dimensional systems.

DOI: [10.1103/PhysRevB.109.125432](https://doi.org/10.1103/PhysRevB.109.125432)

I. INTRODUCTION

Dirac cones, also known as Dirac conical dispersions, prominent in electronic band structures of materials like graphene, yield exceptional electron transport properties [1,2], including quantum Hall effect, *zitterbewegung*, Klein tunneling, etc. It turns out that certain classical wave systems, such as photonic crystals (PhCs), also exhibit Dirac conical dispersions [3–7]. As a photonic analog of graphene, two-dimensional (2D) triangular/honeycomb PhCs have displayed Dirac cones around K and K' points in their band structures, arising from structural symmetry induced mode degeneracy [3–7]. Through accidental degeneracy, conical dispersions distinct from symmetry-protected ones, termed Dirac-like cones, can be engineered in the band structures of PhCs [8–31], which cannot be mapped into the Dirac Hamiltonian and carry zero Berry phase [14]. PhCs possessing a Dirac-like cone at the Brillouin zone center are of particular interest, because they offer a feasible and promising avenue for realizing ultralow-loss zero-index materials (ZIMs) with both effective permittivity and permeability being zero (i.e., $\epsilon_{\text{eff}} = 0$, $\mu_{\text{eff}} = 0$) at the Dirac-point frequency. Such Dirac

cone based ZIMs showcase extraordinary physical properties, and have enabled diverse applications, including cloaking [8,17,18], directive emission [15,16], and photonic doping and antidoping [19–22], as well as exceptional rings and complex Dirac-like cones in non-Hermitian systems [25–28].

By introducing optical anisotropy to PhCs, semi-Dirac cones at the Brillouin zone center, characterized by a unique form of linear-parabolic dispersions resulting from accidental dependency, have been demonstrated [32–38]. The PhCs featuring these semi-Dirac cones exhibit fascinating properties like electromagnetic topological transitions and highly anisotropic electromagnetic responses [32]. More interestingly, they are linked to anisotropic ZIMs, acting as double-zero ZIMs (with $\epsilon_{\text{eff}} = 0$ and $\mu_{\text{eff}} = 0$) along one propagation direction, but single-zero ZIMs (with $\epsilon_{\text{eff}} = 0$ or $\mu_{\text{eff}} = 0$) along the perpendicular direction at the semi-Dirac frequency [32]. This distinctive property has triggered intriguing applications including beam splitters [32,33], directive emission [34,35], asymmetric light transmission [36], cloaking [37], and coherent perfect absorption [38]. However, investigations into the photonic semi-Dirac cones have thus far been confined to 2D systems, leaving the fundamental physics and electromagnetic properties of semi-Dirac cones in three-dimensional (3D) PhCs unexplored.

In this work, we unveil unique band structures—dual semi-Dirac cones in 3D PhCs, which are absent in 2D systems.

*changqing.xu@nnu.edu.cn

†luojie@suda.edu.cn

The dual semi-Dirac cones are the consequences of two sets of triply accidental degeneracy of electric dipolar (ED) and magnetic dipolar (MD) modes within a 3D PhC composed of a simple cubic lattice of core-shell spheroids with a longer semi-axis along the x direction. The dual semi-Dirac dispersion manifests on the $k_x - k_y$ and $k_x - k_z$ planes, while exhibiting triply degenerate Dirac-like dispersion on the $k_y - k_z$ plane. Significantly, these semi-Dirac cones are correlated with topological transitions in equal-frequency contours (EFCs), confirmed by the effective-Hamiltonian and effective-medium descriptions, elucidating drastic changes in electromagnetic responses. We find that the wave transport behaviors within the PhC are highly anisotropic within the frequency region between the two semi-Dirac frequencies. Moreover, at the two semi-Dirac frequencies, the PhC behaves as an effective double-zero ZIM for the y and z propagation directions, but as a single-zero ZIM for the x direction, specifically for orthogonal polarizations. Our work unveils unique band structures in 3D systems, holding potential for advanced electromagnetic wave manipulation.

II. DUAL SEMI-DIRAC CONES AND EIGENMODE ANALYSIS

We start from a 3D PhC composed of a simple cubic lattice of core-shell spheres with a lattice constant of a in air environment, which has been demonstrated to manifest a Dirac-like conical dispersion at the Brillouin center (i.e., the Γ point) [9,22]. The core (radius r_c) and shell (radius r_s) are made of perfect electric conductors (PECs) and dielectrics with relative permittivity ϵ_s , respectively. Figure 1(a) illustrates the PhC unit cell in the left panel, while the middle panel displays the corresponding photonic band structure obtained through finite-element software COMSOL MULTIPHYSICS by solving the following eigenfunction [39]:

$$\nabla \times \left[\frac{1}{\epsilon(\mathbf{r})} \nabla \times \mathbf{H}(\mathbf{r}) \right] = \left(\frac{2\pi f}{c} \right)^2 \mathbf{H}(\mathbf{r}), \quad (1)$$

where $\mathbf{H}(\mathbf{r})$ is the magnetic field, f is the eigenfrequency, c is the speed of light in free space, and $\epsilon(\mathbf{r})$ is the macroscopic dielectric function describing the PhC.

Here the parameters are set as follows: $r_c = 0.0857a$, $r_s = 0.36a$, and $\epsilon_s = 3.15$. The photonic band structure exhibits a pronounced Dirac-like conical dispersion featuring four linear bands and two flat bands around the normalized frequency of $f_D a/c = 0.782$. These bands correspond to three ED modes (upper) and three MD modes (lower) aligned along the x , y , and z directions, as shown in the right panel of Fig. 1(a). The corresponding arrow maps illustrate the electric fields of these modes. The dipolar modes refer to the modes with one nodal plane within the PhC unit cell [39]. The ED mode is characterized by oscillating electric fields along a specific direction, which induces a magnetic current loop. On the other hand, the MD mode is characterized by an electric displacement current loop within the PhC unit cell, which induces a MD moment orthogonal to the current loop [40]. For brevity, we denote the ED (or MD) mode oriented along the i ($i \in x, y, z$) direction as the ED_i (or MD_i) mode. The linear bands correspond to transverse dipolar modes with moment perpendicular to the Bloch wave vector, while the flat bands correspond to

longitudinal dipolar modes. We note that the three ED (or MD) modes are inherently degenerate at the Γ point due to the O_h symmetry of the PhC. However, the degeneracy of ED and MD modes results from the fine tuning of material and structural parameters, finally leading to the formation of an accidentally degenerate Dirac-like point at the Γ point.

Previous studies on 2D PhCs [32–38] suggest that through introducing proper optical anisotropy into the above 3D PhC, the band structure can be reshaped, leading to the transformation of the Dirac-like cone into a semi-Dirac cone. To achieve this, we first alter the external shape of the dielectric shell to a spheroid with semiaxes $r_{sx} \neq r_{sy} = r_{sz}$, resulting in the reduction of the symmetry of the PhC to D_{4h} . Such a spheroid breaks the lattice symmetry along the x and y/z directions, and simultaneously maintains the lattice symmetry along the y and z directions. In this scenario, the original degenerate ED (or MD) modes will split into a single ED_x (or MD_x) mode and doubly degenerate ED_y and ED_z (or MD_y and MD_z) modes. As a result, the Dirac-like cone vanishes along with the linear dispersions. Subsequently, we engineer the structural parameters r_c , r_{sx} , and $r_{sy/sz}$ to reconstruct the accidental degeneracy of ED and MD modes, giving rise to linear dispersions along specific Bloch wave-vector directions. In this way, semi-Dirac cones characterized by linear-parabolic dispersions can be obtained, as demonstrated in the forthcoming examples.

Figure 1(b) shows the first example of the anisotropic 3D PhC, showcasing a semi-Dirac cone achieved through the degeneracy of three orthogonal modes: two ED modes (i.e., ED_z and ED_y) and one MD mode (i.e., MD_x). The relevant structural parameters are set as $r_c = 0.075a$, $r_{sx} = 0.4a$, and $r_{sy} = r_{sz} = 0.32a$, as depicted in the PhC unit cell (left panel). The band structure (middle panel) clearly shows a semi-Dirac cone emerging around the frequency $f_{SD} a/c = 0.807$. In the vicinity of this frequency, dispersion curves consist of two linear bands along the ΓY direction, and two overlapped parabolic bands along the ΓX direction, tangent to a flat band at this frequency. The two linear bands correspond to the transverse ED and MD modes, while the flat band corresponds to the longitudinal mode, as indicated by the arrow maps of electric fields in the right panel. Conversely, the second example in Fig. 1(c) demonstrates a semi-Dirac cone resulting from the triple degeneracy of ED_x , MD_y , and MD_z modes. The left, middle, and right panels display the unit cell (with $r_c = 0.071a$, $r_{sx} = 0.4a$, and $r_{sy} = r_{sz} = 0.32a$), band structure, and the arrow maps of electric fields for the degenerate modes, respectively. Similarly, a semi-Dirac cone comprising two linear bands along the ΓY direction and two overlapped parabolic bands along the ΓX direction, accompanied by a flat band, is obtained at $f_{SD} a/c = 0.792$. Consequently, two distinct types of semi-Dirac cones are realized in 3D anisotropic PhCs.

Now, a crucial question arises: Is it feasible to achieve both types of semi-Dirac cones within a single PhC, thereby realizing dual semi-Dirac cones? The above two examples suggest that there appears to be no inherent physical barrier (e.g., orthogonality of eigenmodes) to achieving this goal. Nevertheless, it remains a very challenging task due to the difficulty of engineering additional modes while simultaneously preserving the existing semi-Dirac cone. Fortunately, through

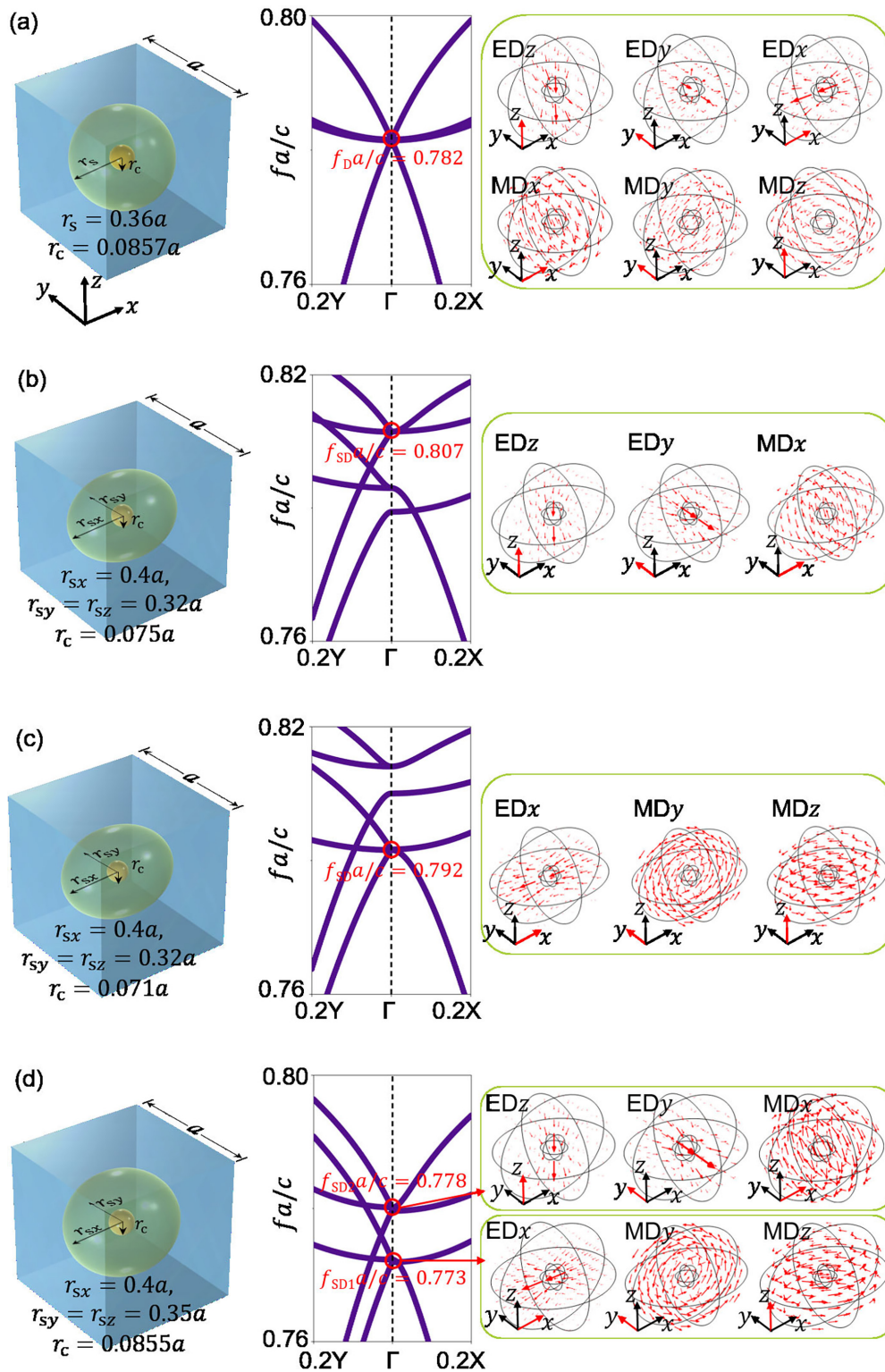


FIG. 1. The unit cell configurations and band structures of 3D cubic-lattice PhCs exhibiting (a) a Dirac-like cone composed of sixfold accidental degeneracy of the ED and MD modes, (b) a single semi-Dirac cone created by triply accidental degeneracy of the EDz, EDy, and MDx modes, (c) a single semi-Dirac cone created by triply accidental degeneracy of the EDx, MDy, and MDz modes, and (d) dual semi-Dirac cones arising from two sets of triply degenerate modes. Left: Illustration of PhC unit cells. Middle: Photonic band structures. Right: Arrow maps of electric fields for the degenerate modes in the ΓY direction with gradually increasing the frequency, close to the Dirac-like and semi-Dirac cones. The axis parallel to the ED or MD moment direction is marked in red.

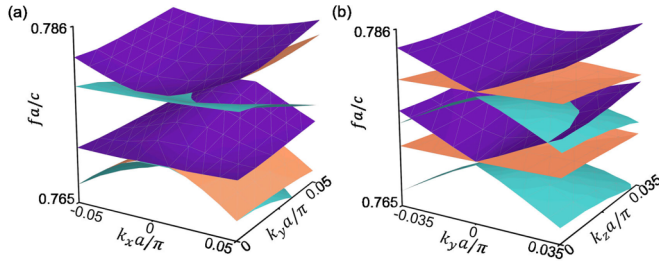


FIG. 2. The dispersion surfaces near the semi-Dirac points on the (a) $k_x - k_y$ and (b) $k_y - k_z$ planes based on the numerical simulations. Different colors are used for a clear illustration of different dispersion surfaces. The dispersion surfaces manifest two semi-Dirac cones on the $k_x - k_y$ plane, and two Dirac-like cones on the $k_y - k_z$ plane.

meticulous parameter optimization, we have successfully designed an anisotropic PhC that exhibits dual semi-Dirac cones. Figure 1(d) shows the unit cell with $r_c = 0.0855a$, $r_{sx} = 0.4a$, and $r_{sy} = r_{sz} = 0.35a$ (left); band structure (middle); and the arrow maps of electric fields for the degenerate modes (right). Notably, two semi-Dirac points emerge at frequencies $f_{SD1}a/c = 0.773$ and $f_{SD2}a/c = 0.778$. Both semi-Dirac cones consist of triply degenerate modes, showcasing linear dispersions along the ΓY direction and parabolic dispersions along the ΓX direction. Importantly, they are created by different modes: the semi-Dirac cone at f_{SD1} results from the accidental degeneracy of ED $_x$, MD $_y$, and MD $_z$ modes, while the semi-Dirac cone at f_{SD2} is created by ED $_z$, ED $_y$, and MD $_x$ modes. This 3D anisotropic PhC unveils unusual band structures that are absent in 2D systems.

Here, it is worth summarizing the design strategy of the PhC exhibiting dual semi-Dirac cones. The utilization of a PEC core offers an additional freedom (i.e., radius r_c) that can effectively engineer dispersions. The PEC core enhances the effective permittivity for ED modes as no electric field is allowed inside it (akin to capacitor models with PEC inclusions), resulting in a reduction of eigenfrequencies of ED modes. Simultaneously, the PEC core imposes zero tangential electric fields on its surface, strongly affecting the loop of electric fields that generates the effective MD moment. Consequently, the eigenfrequencies of MD modes generally increase with increasing r_c . Throughout the design process, meticulous adjustment of four key parameters, i.e., ϵ_s , r_c , r_{sx} , and $r_{sy/sz}$, governs the engineering of ED and MD modes. We find that the modes' order strongly relies on the values of ϵ_s and r_c . The ED modes tend to exhibit higher eigenfrequencies in cases of large ϵ_s , while the MD modes tend to exhibit higher eigenfrequencies in cases of large r_c . Significantly, band flipping behaviors happen during the tuning of these parameters. This enables the proximity of the ED $_x$ (or MD $_x$) mode to the MD $_y/z$ (or ED $_y/z$) mode by choosing appropriate values for ϵ_s and r_c . Subsequently, through comprehensive optimization of all four parameters, the realization of dual semi-Dirac cones is achievable.

III. TOPOLOGICAL TRANSITION AND EFFECTIVE-MEDIUM DESCRIPTION

Figure 2 shows a full view of dispersion surfaces in the vicinity of the two semi-Dirac points in k space. The

dispersion surfaces on the $k_x - k_y$ and $k_y - k_z$ planes are shown in Figs. 2(a) and 2(b), respectively. Linear dispersions along the k_y and k_z directions, but a quadratic dispersion in the k_x direction, at two distinct frequencies, are observed. This signifies the emergence of dual semi-Dirac cones. It is interesting to note that two conical dispersions, arising from triply degenerate modes, are observed on the $k_y - k_z$ plane around the two semi-Dirac points, resembling the Dirac-like cones observed in 2D PhCs [8]. It is noteworthy that these unique dispersions can be elucidated through an effective Hamiltonian on the basis of ED and MD modes [9,13,41] (see Appendix A).

To clearly show the changes in dispersion as the operating frequency varies across the two semi-Dirac points, Fig. 3 displays EFCs for three distinct frequencies $f/c = 0.768, 0.775, 0.782$, delineated by black dashed lines in Fig. 3(a). Figure 3(b) shows the EFCs on the $k_x - k_y$ (left) and $k_y - k_z$ (right) planes. We note that each k plane contains two EFCs associated with orthogonal modes. The numerical labels correspond to bands derived from the band structure in Fig. 3(a). A notable observation is the topological transformation of EFCs on the $k_x - k_y$ plane, transitioning from closed ellipses ($f/c = 0.768$) to open hyperbolas ($f/c = 0.775$), and then returning to closed ellipses again ($f/c = 0.782$). This behavior unveils an intriguing behavior of electromagnetic topological transition [32,42] occurring at the two semi-Dirac points. Such a topological transition is absent for the EFCs on the $k_y - k_z$ plane. Instead, the EFCs tend to coverage towards points at the two semi-Dirac frequencies, indicating the Dirac-like dispersions on the $k_y - k_z$ plane.

The topological transition behavior can also be comprehended based on the effective-medium description. When examining modes nearby the Γ point, the PhC can be characterized by a uniform medium with an effective relative permittivity tensor $\bar{\epsilon}_{\text{eff}} = \begin{pmatrix} \epsilon_{x,\text{eff}} & & \\ & \epsilon_{y,\text{eff}} & \\ & & \epsilon_{z,\text{eff}} \end{pmatrix}$ and an effective relative permeability tensor $\bar{\mu}_{\text{eff}} = \begin{pmatrix} \mu_{x,\text{eff}} & & \\ & \mu_{y,\text{eff}} & \\ & & \mu_{z,\text{eff}} \end{pmatrix}$. Due to structural symmetry, we have $\epsilon_{y,\text{eff}} = \epsilon_{z,\text{eff}}$ and $\mu_{y,\text{eff}} = \mu_{z,\text{eff}}$ at frequencies close to the Γ point. These effective parameters can be determined by matching the dispersion and surface impedance of the corresponding eigenmodes [43,44]. From bands 1 and 3 along the ΓY direction, corresponding to the ED $_x$ and MD $_z$ modes, we obtain $\epsilon_{x,\text{eff}}$ and $\mu_{z,\text{eff}}$ (or $\mu_{y,\text{eff}}$) as follows:

$$\begin{aligned} \epsilon_{x,\text{eff}} &= -\frac{k_y}{Z_{\text{eff}1} \epsilon_0 \omega}, \\ \mu_{z,\text{eff}} &= -\frac{k_y Z_{\text{eff}1}}{\mu_0 \omega} = \mu_{y,\text{eff}}, \end{aligned} \quad (2)$$

where ω is the angular frequency; ϵ_0 and μ_0 are the permittivity and permeability of free space, respectively; $Z_{\text{eff}1} = \langle E_x \rangle / \langle H_z \rangle$ is the effective wave impedance for waves with the electric field polarized along the x direction, propagating along the y direction. The bracket $\langle \dots \rangle$ denotes the average of eigenfields along the xz surface of the PhC unit cell. Similarly,

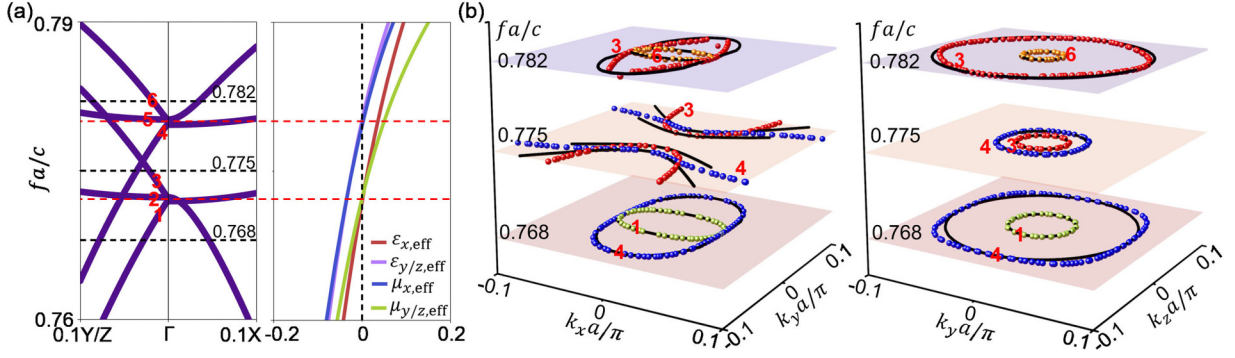


FIG. 3. (a) A zoomed-in view of the dual semi-Dirac conical dispersion (left), and the effective parameters of PhC (right). (b) EFCs at $fa/c = 0.768, 0.775, 0.782$ on the $k_x - k_y$ (left) and $k_y - k_z$ (right) planes. The numerical labels indicate the bands adopted from (a). The dots and lines represent the results from the simulations and analytical dispersions based on effective-medium description, respectively.

from bands 4 and 6, corresponding to the ED_z and MD_x modes, we obtain $\epsilon_{z,\text{eff}}$ (or $\epsilon_{y,\text{eff}}$) and $\mu_{x,\text{eff}}$ as

$$\begin{aligned}\epsilon_{y,\text{eff}} &= \frac{k_y}{Z_{\text{eff}2}\epsilon_0\omega} = \epsilon_{z,\text{eff}} \\ \mu_{x,\text{eff}} &= \frac{k_y Z_{\text{eff}2}}{\mu_0\omega},\end{aligned}\quad (3)$$

where $Z_{\text{eff}2} = \langle E_z \rangle / \langle H_x \rangle$ is the effective wave impedance for waves with the electric field polarized along the z direction, propagating along the y direction.

The effective parameters of the PhC are computed using Eqs. (2) and (3) and are plotted in the right panel of Fig. 3(a). It is observed that the PhC exhibits characteristics of an effective double-zero ZIM with $\epsilon_{x,\text{eff}} = \mu_{z,\text{eff}} = \mu_{y,\text{eff}} = 0$ (or $\epsilon_{y,\text{eff}} = \epsilon_{z,\text{eff}} = \mu_{x,\text{eff}} = 0$) for the y and z propagation directions, but a single-zero ZIM with $\epsilon_{y,\text{eff}}, \epsilon_{z,\text{eff}} \neq 0$ (or $\mu_{y,\text{eff}}, \mu_{z,\text{eff}} \neq 0$) for the x propagation direction at the semi-Dirac frequency $f_{\text{SD}1}$ (or $f_{\text{SD}2}$). This pronounced anisotropic property is expected to induce highly anisotropic wave transport properties for waves of different propagation directions, as elaborated upon in the subsequent section.

Utilizing the effective parameters, the EFCs of the PhC can be well retrieved by the following dispersion relations:

$$\frac{k_x^2}{\mu(\epsilon)_y} + \frac{k_y^2}{\mu(\epsilon)_x} = \epsilon(\mu)_z k_0^2 \quad (4)$$

on the $k_x - k_y$ plane for modes with electric (magnetic) field polarized along the z direction, and

$$\frac{k_y^2}{\mu(\epsilon)_z} + \frac{k_z^2}{\mu(\epsilon)_y} = \epsilon(\mu)_x k_0^2 \quad (5)$$

on the $k_y - k_z$ plane for modes with electric (magnetic) field polarized along the x direction. Here, k_0 is the wave number in free space. The solid lines in Fig. 3(b) depict the retrieved EFCs based on Eqs. (4) and (5), displaying good agreement with the simulation results (dots). The effective parameters shown in Fig. 3(a) reveal that $\mu(\epsilon)_z$, $\mu(\epsilon)_y$, and $\epsilon(\mu)_x$ consistently exhibit the same sign, crossing zero at the same semi-Dirac frequency. As a result, the EFCs on the $k_y - k_z$

plane are always closed circles, exhibiting no topological transition. Interestingly, μ_y and ϵ_z (or ϵ_y and μ_z) have the opposite signs in the frequency region between the two semi-Dirac frequencies (i.e., $f_{\text{SD}1} \sim f_{\text{SD}2}$), resulting in hyperbolic dispersions [45,46], whereas their signs become the same below $f_{\text{SD}1}$ or above $f_{\text{SD}2}$, causing the EFCs to transform into closed ellipses. This change in signs leads to a transition in the topology of the EFCs. These findings underscore that the topological transitions at the two semi-Dirac points can be well characterized by the effective parameters. Importantly, such an effective-medium description significantly simplifies the phenomenological understanding of the PhC, even in the presence of exotic band structures, particularly concerning wave transport properties.

IV. ANISOTROPIC WAVE TRANSPORT PROPERTIES

In the following, we will show the topological transition induced anisotropic wave transport properties within the 3D PhC featuring dual semi-Dirac cones, based on the aforementioned effective-medium description.

We first consider a planar wave propagating along the z direction, where transverse modes that can couple with external waves exist. Figure 4(a) illustrates the configuration, illustrating a planar wave of E_x polarization normally incident onto a PhC slab comprising N_z layers of units along the z direction. Our emphasis here is on the normal incidence to prevent the excitation of longitudinal modes in the flat bands. In this scenario, the incident waves “see” the parameters $\epsilon_{x,\text{eff}}$ and $\mu_{y,\text{eff}}$, both crossing zero at the lower semi-Dirac frequency (i.e., $f_{\text{SD}1}a/c = 0.773$), as demonstrated in Fig. 3(a). This double-zero characteristic is anticipated to lead to robust complete wave transmission [8,21,47]. To validate this expectation, we compute and plot the transmittance spectra for PhC slabs with $N_z = 10, 15, 25$ in Fig. 4(b). Total transmission is observed at $f_{\text{SD}1}$, irrespective of N_z , as shown by the inset. This independence of N_z suggests that the total transmission arises from the double-zero parameters rather than Fabry-Perot resonances. Further evidence is presented in Fig. 4(c), where the upper and lower panels show the distributions of E_x (color) and its phase φ_{E_x} (lines) for a planar wave normally incident on the PhC slab with $N_z = 25$ (upper) and its corresponding effective-medium slab (lower) at $f_{\text{SD}1}$.

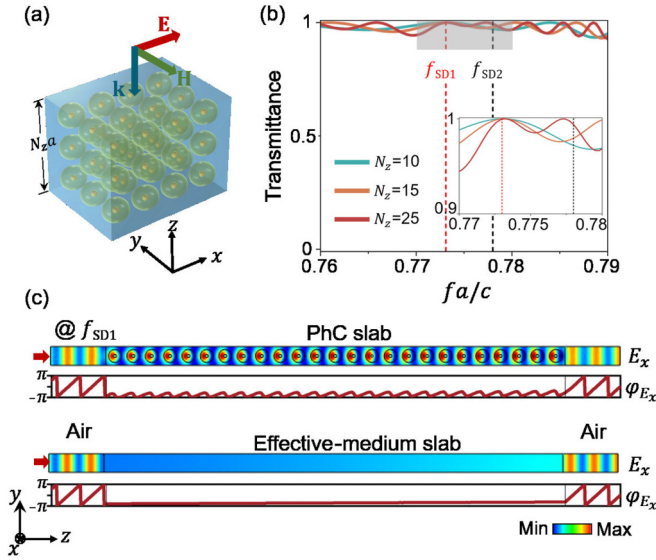


FIG. 4. (a) Schematic graph of a planar wave of E_x polarization propagating along the z direction normally incident on a PhC slab consisting of N_z layers of units along the z direction. (b) Transmittance spectra for PhC slabs with $N_z = 10, 15, 25$. The dashed lines mark the two semi-Dirac frequencies. The inset is the magnification of the gray region. (c) Distributions of E_x and its phase φ_{E_x} (lines) for the planar wave normally incident on the PhC slab with $N_z = 25$ (upper) and its corresponding effective-medium slab (lower) at the lower semi-Dirac frequency $f_{SD1}a/c = 0.773$.

These results exhibit good agreement, showing a small phase change ($\sim 0.2\pi$) over a long propagation distance of $25a$ ($\sim 19\lambda_0$), further confirming the double-zero characteristic of the PhC for waves of E_x polarization propagating along the z direction at the lower semi-Dirac frequency f_{SD1} .

Then we alter the polarization direction of the incident wave to the y direction, while maintaining the propagation direction unchanged, as illustrated in Fig. 5(a). In this scenario, the wave transport characteristics are governed by the parameters $\varepsilon_{y,\text{eff}}$ and $\mu_{x,\text{eff}}$. Referring to Fig. 3(a), we observe that the two parameters simultaneously cross zero at the upper semi-Dirac frequency (i.e., $f_{SD2}a/c = 0.778$). Consequently, we anticipate N_z -independent complete transmission to occur at f_{SD2} , as validated by the transmittance spectra in Fig. 5(b). The distributions of E_y (color) and its phase φ_{E_y} (lines) for the planar wave normally incident on the PhC slab with $N_z = 25$ and its corresponding effective-medium slab at f_{SD2} [Fig. 5(c)] show nearly perfect transmission and a small phase lag ($\sim 0.2\pi$), providing further evidence of the double-zero characteristic of the PhC for waves of E_y polarization at the upper semi-Dirac frequency f_{SD2} .

These findings demonstrate that the 3D PhC functions as an effective double-zero ZIM at the semi-Dirac frequencies, specifically for orthogonal polarizations, along the z propagation direction. Due to structural symmetry, a similar double-zero characteristic is expected for the y propagation direction. Analyzing the effective parameters in Fig. 3(a), we can infer that the 3D PhC acts as an effective double-zero ZIM for waves of E_x polarization at f_{SD1} , while for waves

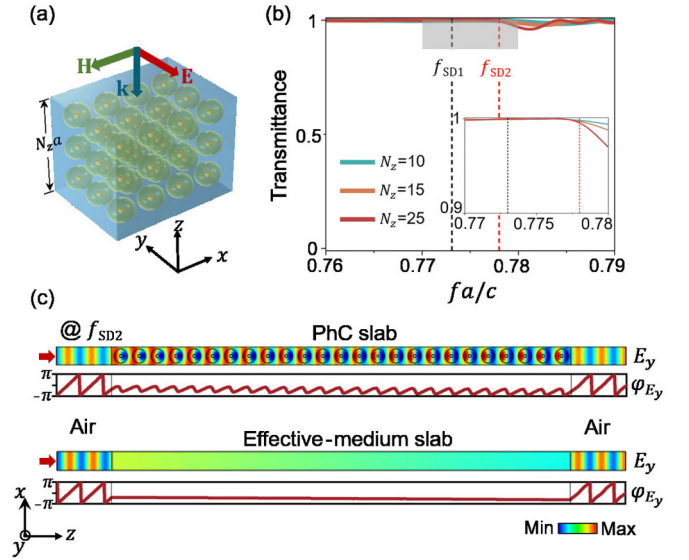


FIG. 5. (a) Schematic graph of a planar wave of E_y polarization propagating along the z direction normally incident on a PhC slab consisting of N_z layers of units along the z direction. (b) Transmittance spectra for PhC slabs with $N_z = 10, 15, 25$. The dashed lines mark the two semi-Dirac frequencies. The inset is the magnification of the gray region. (c) Distributions of E_y and its phase φ_{E_y} (lines) for a planar wave normally incident on the PhC slab with $N_z = 25$ (upper) and its corresponding effective-medium slab (lower) at the upper semi-Dirac frequency $f_{SD2}a/c = 0.778$.

of E_z polarization at f_{SD2} , the 3D PhC acts as an effective double-zero ZIM along the y propagation direction.

It is important to highlight that the PhC slabs exhibit high transmittance (>0.9) independent of N_z across the entire studied frequency spectrum (i.e., $fa/c = 0.76\text{--}0.79$) for both models in Figs. 4 and 5. This is because the PhC is almost impedance matched with free space within this frequency region. Actually, our numerical calculations (not shown here) reveal that the bandwidth of this robust high transmission is very broad, roughly covering the frequency range of $fa/c = 0.51\text{--}0.83$ for both models in Figs. 4 and 5. This indicates that the PhC can function as an effective wave-transparent metastructure, despite being constructed from reflective dielectrics and PECs. Such characteristics hold promising potential for practical applications in areas such as radomes and wireless communications.

Notably, the wave transport characteristics undergo a profound transformation when the propagation direction is altered to the x direction, as schematically shown in Fig. 6(a). A planar wave of E_z polarization is normally incident on the PhC slab comprising N_x layers of units along the x direction. The transmittance spectra for PhC slabs with $N_x = 10, 15, 25$ are presented in Fig. 6(b). It is seen that the transmission experiences a rapid decline in the vicinity of the two semi-Dirac frequencies with increasing N_x , showcasing distinct wave transport behaviors compared to the cases involving the z propagation direction. Such a substantial change is foreseeable due to the asymmetric band structures along the x and y (or z) directions nearby the two semi-Dirac frequencies. Particularly, topological transitions of EFCs occur at the two

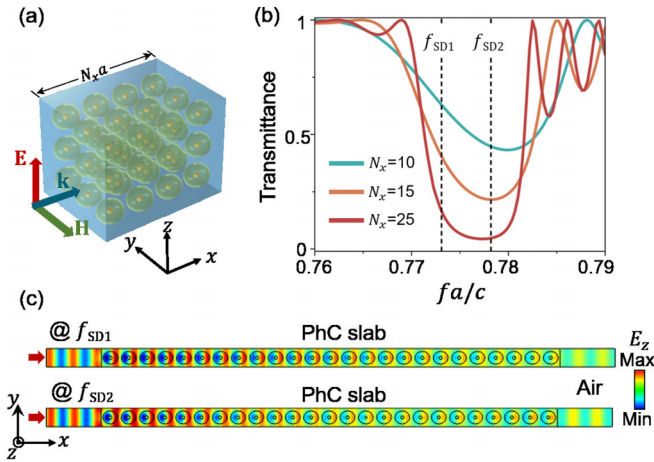


FIG. 6. (a) Schematic graph of a planar wave of E_z polarization propagating along the x direction normally incident onto a PhC slab consisting of N_x layers of units along the x direction. (b) Transmittance spectra for PhC slabs with $N_x = 10, 15, 25$. The dashed lines mark the two semi-Dirac frequencies. (c) Distributions of E_z for a planar wave normally incident onto the PhC slab with $N_x = 25$ at $f_{SD1}a/c = 0.773$ (upper) and $f_{SD2}a/c = 0.778$ (lower).

semi-Dirac frequencies, forming a directional band gap along the ΓX direction within the frequency range of $f_{SD1} - f_{SD2}$. The change in wave transport property can also be comprehended from the perspective of effective parameters. In this scenario, the wave transport property is influenced by the parameters $\mu_{y,\text{eff}}$ and $\varepsilon_{z,\text{eff}}$. Referring to Fig. 3(a), we observe that $\mu_{y,\text{eff}} \sim 0$ and $\varepsilon_{z,\text{eff}} < 0$ (or $\varepsilon_{z,\text{eff}} \sim 0$ and $\mu_{y,\text{eff}} > 0$) at the lower (or upper) semi-Dirac frequency, where the PhC behaves as a single-zero ZIM. It was demonstrated that the wave transmission decreases with increasing the thickness of the single-zero ZIM [47,48], as evident in the electric-field distributions shown in Fig. 6(c). Within the frequency range of $f_{SD1} - f_{SD2}$, we have $\varepsilon_{z,\text{eff}} < 0$ and $\mu_{y,\text{eff}} > 0$, indicating that the PhC behaves as a single-negative material. Waves inside it become evanescent, resulting in low transmission, especially for a large slab thickness (i.e., a large layer number N_x). We note that a similar wave transport behavior is anticipated for waves of E_y polarization, as deduced from the effective parameters.

Overall, topological transition induced anisotropic wave transport behaviors are demonstrated within the 3D PhC featuring dual semi-Dirac cones. The PhC exhibits drastically different wave transport properties for waves of different propagation directions in the vicinity of semi-Dirac frequencies. For the y/z propagation direction, the PhC behaves as an effective double-zero ZIM with broadband robust wave transparency at the semi-Dirac frequencies. In contrast, for the x propagation direction, it behaves as a single-zero ZIM at the semi-Dirac frequencies, and a single-negative material between the two semi-Dirac frequencies due to the directional band gap, thus leading to low wave transmission. These

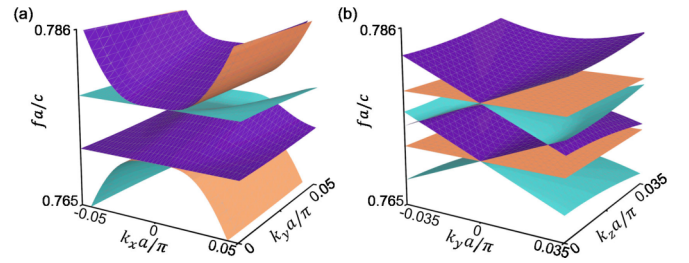


FIG. 7. The dispersion surfaces near the semi-Dirac points on the (a) $k_x - k_y$ and (b) $k_y - k_z$ planes based on the effective Hamiltonian $H_{SD, \text{eff}}$.

findings underscore the significant impact of topological transitions on wave transport properties of the 3D PhC.

V. DISCUSSION AND CONCLUSION

Finally, it is crucial to emphasize that the studied 3D systems offer an additional degree of freedom for manipulating band structures compared to 2D systems. This presents a viable avenue for constructing exotic dispersions that are absent in 2D systems. As demonstrated in the aforementioned 3D PhC, it showcases dual semi-Dirac cones on the $k_x - k_y$ and $k_x - k_z$ planes, while two sets of triply accidentally degenerate Dirac-like cones on the $k_y - k_z$ plane. This suggests the potential to unveil more exotic dispersions in 3D PhCs due to the increased degree of freedom inherent in 3D systems.

In summary, we have demonstrated the unique dual semi-Dirac cones in 3D PhCs, arising from two sets of triply accidental degeneracy of ED and MD modes. The identification of these two semi-Dirac cones is linked to topological transitions in EFCs, as substantiated by both the effective-Hamiltonian and effective-medium descriptions. Highly anisotropic wave transport properties triggered by the topological transitions are further demonstrated. Our findings apply to dispersionless and lossless materials. The introduction of material dispersion and losses could affect the mode degeneracy. Their influences on the accidentally degenerate semi-Dirac cones remain uncertain, and worthy of further exploration.

Data underlying the results presented in this paper are not publicly available at this time but may be obtained from the authors upon reasonable request.

ACKNOWLEDGMENTS

This work was supported by the National Key R&D Program of China (Grant No. 2022YFA1404301), the National Natural Science Foundation of China (Grants No. 12374293, No. 11974010, and No. 12274313), the Natural Science Foundation of Jiangsu Province (Grant No. BK20221354), and the Undergraduate Training Program for Innovation and Entrepreneurship, Soochow University. C.X. was supported by the Jiangsu Specially Appointed Professor Program (Grant No. 164080H00244).

The authors declare no conflicts of interest.

APPENDIX A: EFFECTIVE-HAMILTONIAN DESCRIPTION

The effective Hamiltonian of the proposed 3D PhC can be formulated on the basis of ED and MD modes as [9,13,41]

$$H_{D, \text{eff}} = \begin{pmatrix} \omega_{ex} & 0 & 0 & 0 & ipk_z & -ipk_y \\ 0 & \omega_{ey} & 0 & -ipk_z & 0 & ipk_x \\ 0 & 0 & \omega_{ez} & ipk_y & -ipk_x & 0 \\ 0 & ip^*k_z & -ip^*k_y & \omega_{mx} & 0 & 0 \\ -ip^*k_z & 0 & ip^*k_x & 0 & \omega_{my} & 0 \\ ip^*k_y & -ip^*k_x & 0 & 0 & 0 & \omega_{mz} \end{pmatrix}, \quad (\text{A1})$$

where ω_{ei} and ω_{mi} ($i \in x, y, z$) are associated with the energy of the ED i and MD i modes, respectively; p represents the coefficient of the first order of dispersions; and for conciseness, the lattice constant is set to be unity. The accidental degeneracy of the ED and MD modes at the Brillouin zone center implies $\omega_{ei} = \omega_{mi}$ at the Dirac-point frequency ω_D . Under this circumstance, the six eigenvalues of the Hamiltonian $H_{D, \text{eff}}$ are

$$\begin{aligned} \omega_1 &= \omega_2 = \omega_D, \\ \omega_3 &= \omega_4 = \omega_D + |p||\mathbf{k}|, \\ \omega_5 &= \omega_6 = \omega_D - |p||\mathbf{k}|, \end{aligned} \quad (\text{A2})$$

indicating the presence of two flat bands (ω_1 and ω_2) and four linear bands (ω_3 to ω_6) in the vicinity of the Γ point. In the scenario where the sixfold Dirac-like point is gapped into two semi-Dirac points [Fig. 1(d)], the effective Hamiltonian can be rewritten as

$$H_{SD, \text{eff}} = \begin{pmatrix} \omega_{SD1} & 0 & 0 & 0 & ip'k_z & -ip'k_y \\ 0 & \omega_{SD2} & 0 & -ip'k_z & 0 & iqk_x^2 \\ 0 & 0 & \omega_{SD2} & ip'k_y & -iqk_x^2 & 0 \\ 0 & ip^*k_z & -ip^*k_y & \omega_{SD2} & 0 & 0 \\ -ip^*k_z & 0 & iq^*k_x^2 & 0 & \omega_{SD1} & 0 \\ ip^*k_y & -iq^*k_x^2 & 0 & 0 & 0 & \omega_{SD1} \end{pmatrix}, \quad (\text{A3})$$

where p' is the coefficient of the first order of dispersions along the k_y and k_z directions; q is the coefficient of the second order of dispersions along the k_x direction. At the Γ point, the accidental degeneracy of the ED x , MD y , and MD z modes occurs at ω_{SD1} ; meanwhile, the accidental degeneracy of the ED z , ED y , and MD x modes occurs at ω_{SD2} . In this case, the eigenvalues of the Hamiltonian $H_{SD, \text{eff}}$ are

$$\begin{aligned} \omega_1 &= \omega_{SD1}, \\ \omega_2 &= \omega_{SD1} - \sqrt{q^2k_x^4 + p^2(k_y^2 + k_z^2)}, \\ \omega_3 &= \omega_{SD1} + \sqrt{q^2k_x^4 + p^2(k_y^2 + k_z^2)}, \\ \omega_4 &= \omega_{SD2}, \\ \omega_5 &= \omega_{SD2} - \sqrt{q^2k_x^4 + p^2(k_y^2 + k_z^2)}, \\ \omega_6 &= \omega_{SD2} + \sqrt{q^2k_x^4 + p^2(k_y^2 + k_z^2)}. \end{aligned} \quad (\text{A4})$$

Equation (A4) reveals the presence of two flat bands (ω_1 and ω_4) and four exotic bands (ω_2 , ω_3 , ω_5 , and ω_6). Notably, these exotic bands exhibit a linear behavior along the k_y direction ($k_x = k_z = 0$) and k_z direction ($k_x = k_y = 0$), but a quadratic behavior along the k_x direction ($k_y = k_z = 0$). This signifies the emergence of dual semi-Dirac cones.

For visualization, the analytical dispersion surfaces on the $k_x - k_y$ and $k_y - k_z$ planes in the vicinity of the two semi-Dirac points using Eq. (A4) are plotted in Figs. 7(a) and 7(b), respectively. They agree well with the simulation results in Fig. 2, validating the effectiveness of the Hamiltonian description. Analysis of the dispersion surfaces reveals linear dispersions along the k_y and k_z directions, but a quadratic dispersion in the k_x direction, at two distinct frequencies, thereby confirming the presence of dual semi-Dirac cones.

APPENDIX B: METHODS OF SIMULATION

Numerical simulations are performed using the finite-element software COMSOL MULTIPHYSICS. The band structures and EFCs in Figs. 1–3 are calculated using a continuum Floquet eigensolver with Floquet periodic boundary conditions. The eigenfrequencies can be calculated for given Bloch wave vectors. The transmittance spectra and field distributions in Figs. 4–6 are obtained by full-wave simulations in the frequency domain. The upper and lower boundaries of the models in Figs. 4(c), 5(c), and 6(c) are set as Floquet periodic boundaries. The left and right boundaries are set as port, which are used to excite the incident wave and absorb the transmitted wave. The transmittance spectra are retrieved from S parameters of the ports.

- [1] A. K. Geim and K. S. Novoselov, The rise of graphene, *Nat. Mater.* **6**, 183 (2007).
- [2] A. H. Castro Neto, F. Guinea, N. M. R. Peres, K. S. Novoselov, and A. K. Geim, The electronic properties of graphene, *Rev. Mod. Phys.* **81**, 109 (2009).
- [3] M. Plihal and A. Maradudin, Photonic band structure of two-dimensional systems: The triangular lattice, *Phys. Rev. B* **44**, 8565 (1991).
- [4] O. Peleg, G. Bartal, B. Freedman, O. Manela, M. Segev, and D. N. Christodoulides, Conical diffraction and gap solitons in honeycomb photonic lattices, *Phys. Rev. Lett.* **98**, 103901 (2007).
- [5] X. Zhang, Observing *Zitterbewegung* for photons near the Dirac point of a two-dimensional photonic crystal, *Phys. Rev. Lett.* **100**, 113903 (2008).
- [6] T. Ochiai and M. Onoda, Photonic analog of graphene model and its extension: Dirac cone, symmetry, and edge states, *Phys. Rev. B* **80**, 155103 (2009).
- [7] D. Dragoman and M. Dragoman, Analogies for Dirac fermions physics in graphene, *Solid State Electron.* **211**, 108818 (2024).
- [8] X. Huang, Y. Lai, Z. H. Hang, H. Zheng, and C. T. Chan, Dirac cones induced by accidental degeneracy in photonic crystals and zero-refractive-index materials, *Nat. Mater.* **10**, 582 (2011).
- [9] C. T. Chan, X. Huang, F. Liu, and Z. H. Hang, Dirac dispersion and zero-index in two dimensional and three dimensional photonic and phononic systems, *Prog. Electromagn. Res. B* **44**, 164 (2012).
- [10] J. Luo and Y. Lai, Hermitian and non-Hermitian Dirac-like cones in photonic and phononic structures, *Front. Phys.* **10**, 845624 (2022).
- [11] D. I. Vulis, O. Reshef, P. Camayd-Muñoz, and E. Mazur, Manipulating the flow of light using Dirac-cone zero-index metamaterials, *Rep. Prog. Phys.* **82**, 012001 (2019).
- [12] Y. Li, C. T. Chan, and E. Mazur, Dirac-like cone-based electromagnetic zero-index metamaterials, *Light: Sci. Appl.* **10**, 203 (2021).
- [13] K. Sakoda, Proof of the universality of mode symmetries in creating photonic Dirac cones, *Opt. Express* **20**, 25181 (2012).
- [14] J. Mei, Y. Wu, C. T. Chan, and Z. Zhang, First-principles study of Dirac and Dirac-like cones in phononic and photonic crystals, *Phys. Rev. B* **86**, 035141 (2012).
- [15] P. Moitra, Y. Yang, Z. Anderson, I. I. Kravchenko, D. P. Briggs, and J. Valentine, Realization of an all-dielectric zero-index optical metamaterial, *Nat. Photon.* **7**, 791 (2013).
- [16] Y. Li, S. Kita, P. Muñoz, O. Reshef, D. I. Vulis, M. Yin, M. Lončar, and E. Mazur, On-chip zero-index metamaterials, *Nat. Photon.* **9**, 738 (2015).
- [17] J. Dong, M. Chang, X. Huang, Z. H. Hang, Z. Zhong, W. Chen, Z. Huang, and C. T. Chan, Conical dispersion and effective zero refractive index in photonic quasicrystals, *Phys. Rev. Lett.* **114**, 163901 (2015).
- [18] H. Chu, Q. Li, B. Liu, J. Luo, S. Sun, Z. H. Hang, L. Zhou, and Y. Lai, A hybrid invisibility cloak based on integration of transparent metasurfaces and zero-index materials, *Light: Sci. Appl.* **7**, 50 (2018).
- [19] J. Luo, B. Liu, Z. H. Hang, and Y. Lai, Coherent perfect absorption via photonic doping of zero-index media, *Laser Photon. Rev.* **12**, 1800001 (2018).
- [20] D. Wang, J. Luo, Z. Sun, and Y. Lai, Transforming zero-index media into geometry-invariant coherent perfect absorbers via embedded conductive films, *Opt. Express* **29**, 5247 (2021).
- [21] C. Xu, H. Chu, J. Luo, Z. H. Hang, Y. Wu, and Y. Lai, Three-dimensional electromagnetic void space, *Phys. Rev. Lett.* **127**, 123902 (2021).
- [22] D. Yan, R. Mei, M. Li, Z. Ma, Z. H. Hang, and J. Luo, Controlling coherent perfect absorption via long-range connectivity of defects in three-dimensional zero-index media, *Nanophotonics* **12**, 4205 (2023).
- [23] C. Xu and Y. Lai, Configurable Dirac-like conical dispersions in complex photonic crystals, *Phys. Rev. B* **95**, 045124 (2017).
- [24] D. Yang, F. Feng, L. Sun, N. Wang, and G. P. Wang, Realization of magneto-optical near-zero-index metamaterial by using an array of spinning cylinders, *Phys. Rev. A* **105**, 043517 (2022).
- [25] B. Zhen, C. W. Hsu, Y. Igarashi, L. Lu, I. Kaminer, A. Pick, S. Chua, J. D. Joannopoulos, and M. Soljačić, Spawning rings of exceptional points out of Dirac cones, *Nature (London)* **525**, 354 (2015).
- [26] Z. Lin, A. Pick, M. Lončar, and A. W. Rodriguez, Enhanced spontaneous emission at third-order Dirac exceptional points in inverse-designed photonic crystals, *Phys. Rev. Lett.* **117**, 107402 (2016).
- [27] L. Luo, Y. Shao, J. Li, R. Fan, R. Peng, M. Wang, J. Luo, and Y. Lai, Non-Hermitian effective medium theory and complex Dirac-like cones, *Opt. Express* **29**, 14345 (2021).
- [28] C. Xu, M. Farhat, and Y. Wu, Non-Hermitian electromagnetic double-near-zero index medium in a two-dimensional photonic crystal, *Appl. Phys. Lett.* **119**, 224102 (2021).
- [29] M. Minkov, I. A. D. Williamson, M. Xiao, and S. Fan, Zero-index bound states in the continuum, *Phys. Rev. Lett.* **121**, 263901 (2018).
- [30] T. Dong, J. Liang, S. Camayd-Muñoz, Y. Liu, H. Tang, S. Kita, P. Chen, X. Wu, W. Chu, E. Mazur, and Y. Li, Ultra-low-loss on-chip zero-index materials, *Light: Sci. Appl.* **10**, 10 (2021).
- [31] H. Tang, C. DeVault, S. A. Camayd-Muñoz, Y. Liu, D. Jia, F. Du, O. Mello, D. I. Vulis, Y. Li, and E. Mazur, Low-loss zero-index materials, *Nano Lett.* **21**, 914 (2021).
- [32] Y. Wu, A semi-Dirac point and an electromagnetic topological transition in a dielectric photonic crystal, *Opt. Express* **22**, 1906 (2014).
- [33] U. G. Yasa, M. Turdueva, I. H. Giden, and H. Kurt, Full utilization of semi-Dirac cones in photonics, *Phys. Rev. B* **97**, 195131 (2018).
- [34] X. He, Y. Zhong, Y. Zhou, Z. Zhong, and J. Dong, Dirac directional emission in anisotropic zero refractive index photonic crystals, *Sci. Rep.* **5**, 13085 (2015).
- [35] L. Vertchenko, C. DeVault, R. Malureanu, E. Mazur, and A. Lavrinenko, Near-zero index photonic crystals with directive bound states in the continuum, *Laser Photon. Rev.* **15**, 2000559 (2021).
- [36] E. Bor, M. Turdueva, U. G. Yasa, H. Kurt, and K. Staliunas, Asymmetric light transmission effect based on an evolutionary optimized semi-Dirac cone dispersion photonic structure, *Phys. Rev. B* **98**, 245112 (2018).
- [37] E. Bor, U. Gorkem Yasa, H. Kurt, and M. Turdueva, Demonstration of carpet cloaking by an anisotropic zero refractive index medium, *Opt. Lett.* **45**, 2423 (2020).
- [38] Z. Li, H. Lin, R. Tang, H. Chen, J. Tang, R. Zhou, J. Jin, and Y. Liu, Coherent perfect absorber and laser induced by directional

- emissions in the non-Hermitian photonic crystals, *Opt. Express* **31**, 41276 (2023).
- [39] J. D. Joannopoulos, S. G. Johnson, J. N. Winn, and R. D. Meade, *Photonic Crystals: Molding the Flow of Light*, 2nd ed. (Princeton University Press, Princeton, NJ, 2008).
- [40] M. A. van de Haar, J. van de Groep, B. J. M. Brenny, and A. Polman, Controlling magnetic and electric dipole modes in hollow silicon nanocylinders, *Opt. Express* **24**, 2047 (2016).
- [41] C. Guo, V. S. Asadchy, B. Zhao, and S. Fan, Light control with Weyl semimetals, *eLight* **3**, 2 (2023).
- [42] H. N. Krishnamoorthy, Z. Jacob, E. Narimanov, I. Kretzschmar, and V. M. Menon, Topological transitions in metamaterials, *Science* **336**, 205 (2012).
- [43] J. Luo, Y. Yang, Z. Yao, W. Lu, B. Hou, Z. H. Hang, C. T. Chan, and Y. Lai, Ultratransparent media and transformation optics with shifted spatial dispersions, *Phys. Rev. Lett.* **117**, 223901 (2016).
- [44] S. Li, Y. Wang, W. Zhang, W. Lu, B. Hou, J. Luo, and Y. Lai, Observation of wide-angle impedance matching in terahertz photonic crystals, *New J. Phys.* **22**, 023033 (2020).
- [45] A. Poddubny, I. Iorsh, P. Belov, and Y. Kivshar, Hyperbolic metamaterials, *Nat. Photon.* **7**, 948 (2013).
- [46] D. Lee, S. So, G. Hu, M. Kim, T. Badloe, H. Cho, J. Kim, H. Kim, C. Qiu, and J. Rho, Hyperbolic metamaterials: Fusing artificial structures to natural 2D materials, *eLight* **2**, 1 (2022).
- [47] J. Luo and Y. Lai, Epsilon-near-zero or mu-near-zero materials composed of dielectric photonic crystals, *Sci. China Inf. Sci.* **56**, 1 (2013).
- [48] A. Alù, M. Silveirinha, A. Salandrino, and N. Engheta, Epsilon-near-zero metamaterials and electromagnetic sources: Tailoring the radiation phase pattern, *Phys. Rev. B* **75**, 155410 (2007).